

Fourier-enhanced reduced-order surrogate modeling for uncertainty quantification in electric machine design

Aylar Partovizadeh^{1,2,*}, Sebastian Schöps ^{1,2,3}, and Dimitrios Loukrezis ^{2,3}

¹Computational Electromagnetics Group, Technische Universität Darmstadt
Schloßgartenstr. 8, 64289 Darmstadt, Germany

²Institute for Accelerator Science and Electromagnetic Fields, Technische Universität Darmstadt
Schloßgartenstr. 8, 64289 Darmstadt, Germany

³Graduate School of Computational Engineering, Technische Universität Darmstadt
Dolivostr. 15, 64293 Darmstadt, Germany

*Corresponding author: aylar.partovizadeh@tu-darmstadt.de

Contributing authors: sebastian.schoeps@tu-darmstadt.de, dimitrios.loukrezis@tu-darmstadt.de

Abstract

This work proposes a data-driven surrogate modeling framework for cost-effectively inferring the torque of a permanent magnet synchronous machine under geometric design variations. The framework is separated into a reduced-order modeling and an inference part. Given a dataset of torque signals, each corresponding to a different set of design parameters, torque dimension is first reduced by post-processing a discrete Fourier transform and keeping a reduced number of frequency components. This allows to take advantage of torque periodicity and preserve physical information contained in the frequency components. Next, a response surface model is computed by means of machine learning regression, which maps the design parameters to the reduced frequency components. The response surface models of choice are polynomial chaos expansions, feedforward neural networks, and Gaussian processes. Torque inference is performed by evaluating the response surface model for new design parameters and then inverting the dimension reduction. Numerical results show that the resulting surrogate models lead to sufficiently accurate torque predictions for previously unseen design configurations. The framework is found to be significantly advantageous compared to approximating the original (not reduced) torque signal directly, as well as slightly advantageous compared to using principal component analysis for dimension reduction. The combination of discrete Fourier transform-based dimension reduction with Gaussian process-based response surfaces yields the best-in-class surrogate model for this use case. The surrogate models replace the original, high-fidelity model in Monte Carlo-based uncertainty quantification studies, where they provide accurate torque statistics estimates at significantly reduced computational cost.

Keywords: dimension reduction, discrete Fourier transform, electric machine design, machine learning regression, permanent magnet synchronous machine, reduced-order model, response surface, surrogate model, uncertainty quantification.

1. Introduction

Several sectors of major societal and economic interest, such as industry, infrastructure, and transportation, currently undergo transformative changes towards their electrification [1]. These changes drive an ever increasing usage of electric machines, which in turn imposes high demands on design quality and reliability. Considering computer-aided design (CAD) in particular, discrepancies between computer models and manufactured machines are all but inevitable, often affecting crucial quantities of interest (QoIs) [2].

To a large extent, these discrepancies can be attributed to *epistemic* uncertainty, referring to systematic modeling errors due to inexactly known physical mechanisms, or *aleatory* uncertainty, referring to inherently random variations in the design parameters [3]. This work focuses on aleatory uncertainty only. In this context, uncertainty quantification (UQ) aims at assessing the impact of random design parameters upon QoIs [4], such that more robust and reliable designs may be developed. However, workhorse UQ methods such as Monte Carlo sampling [5] can incur severe computational costs, due to their need for numerous evaluations of possibly time and resource-demanding numerical models and simulations, as is also the case in electric machine design.

A common way to mitigate the computational cost of UQ - or other studies that require repetitive model evaluations for varying parameter values, such as optimization or design exploration - is to replace the computationally demanding, high-fidelity model with an inexpensive albeit sufficiently accurate *surrogate* model [6]. A surrogate modeling approach that dates back to the work of Box and Wilson in the early 1950s, is to use a dataset of model parameters and corresponding QoI values to establish a so-called response surface model (RSM) that mimics the functional relation between parameters and QoI [7]. Among other options, polynomial chaos expansions (PCEs), feedforward neural networks (FNNs), and Gaussian processes (GPs) have been routinely used as RSMs [8–13]. An alternative approach is to decrease the cost of a computational model by reducing the dimensionality of the algebraic objects encountered in its numerical solution, resulting in a so-called reduced-order model (ROM). Depending on application and ROM method of choice, dimension reduction can be applied to the input parameters, the QoI, the system matrices of the numerical model, or combinations thereof. This typically entails computing an approximate, low-dimensional representation of the original, high-dimensional algebraic object, using methods such as balanced truncation, proper orthogonal decomposition, Krylov subspaces, tensor decompositions, or dynamic mode decomposition, to name but a few relevant options [14–17]. As a natural extension, surrogate modeling methods that combine ROMs with RSMs have also been developed [18–20]. Note that the literature does not always clearly distinguish between ROMs and surrogate models, even using the terms interchangeably on occasion. In the context of this work, these terms will be used as described above.

The present work focuses on the design of a permanent magnet synchronous machine (PMSM) under geometrical variations, possibly random ones. Different PMSM geometries are obtained by varying 20 parameters of a CAD model [21], which take values within predefined ranges. The considered QoI is the electromagnetic torque developed during the machine’s rotation, which is computed using a numerical model based on isogeometric analysis (IGA) [22]. For the torque signal to have sufficient resolution, e.g., to account for so-called torque ripples, the torque must be evaluated for a large number of rotation angles, thus resulting in a high-dimensional QoI. The high dimensionality of the QoI can hinder the application of direct surrogate modeling approaches, such as RSMs mapping the design parameters to the QoI, by increasing computation time and failing to reach sufficient approximation accuracy. An obvious solution is to use a dimension reduction method upon the torque signal. However, common methods do not take into account important properties of the torque signal, such as periodicity (for steady-state operation) and frequency content.

To compute a sufficiently accurate surrogate model that predicts the torque of the PMSM given different geometrical designs and thus enable UQ studies, this work suggests a data-driven surrogate modeling framework utilizing discrete Fourier transform (DFT) for dimension reduction in combination with RSMs. The framework is separated into a reduced-order modeling part and an inference part. For reduced-order modeling, DFT is first applied to a dataset of torque signals, each obtained for different design parameters. Next, critical frequency components are retained while the rest are omitted, resulting in a reduced QoI that preserves the most important frequency content of the signal. Then, machine learning (ML) regression is used to compute an RSM that maps the design parameters to the reduced frequency components. To infer the torque given a new geometrical design of the PMSM, the RSM is first evaluated, followed by inverting the DFT, thus obtaining the full torque signal.

From a methodological perspective, the use of DFT for the purpose of dimension reduction and its utilization in a surrogate modeling context is the main novelty of the suggested framework. The review of Hou and Behdinan [23] lists several prior works which have pursued similar ideas, wherein DFT-based dimension reduction is not included. For this particular use case, DFT ensures that important physical information contained in the frequency components is retained, thus leading to superior results in terms of surrogate modeling accuracy, as also supported by the numerical studies available in this work. The use of a reduced-order surrogate model, i.e., one that integrates dimension reduction of the QoI in combination with an RSM, is also a novel contribution concerning surrogate-assisted electric machine design, see for example the review of Cheng et al. [24] and the references therein. Last, contrary to most works encountered in the literature, the suggested framework is not restricted to a single RSM. Instead, different RSM options are evaluated, namely, PCE, FNN, and GP, in an attempt to identify the best-in-class surrogate model for this use case.

The remaining of this paper is organized as follows. Section 2 presents the PMSM model, its numerical approximation, and the considered geometrical variations. Next, the data-driven reduced-order surrogate modeling framework proposed in this work is detailed in section 3. Numerical studies regarding the performance of surrogate models obtained with the suggested framework are presented in section 4. Last, section 5 contains concluding remarks.

2. Problem setting: PMSM with geometry variations

2.1 Geometry representation in CAD

We consider a PMSM similar to the one depicted in Figure 1, where only one-fourth of a two-dimensional cross-section of its geometry is shown, taking into account rotational symmetry and translational invariance. The PMSM consists of a stator and a rotor, separated by an air gap. The rotor is composed of an iron part, permanent magnets, and air slots. The stator comprises an iron part and six slots where the copper windings carrying the source current are placed. For computational purposes, the air gap is divided into a rotor part and a stator part, separated by the interface Γ_{ag} . This is a benchmark PMSM geometry obtained from the commercial software JMAG [25]. For the purposes of the present study, the geometry is rebuilt using the GeopDEs software [26, 27].

As is common in CAD, the PMSM's geometry is parametrized using free-form curves, such that the geometry is defined through a projection map from a reference domain $[0, 1]^d$ to the physical domain $\Omega \subset \mathbb{R}^r$, $r \geq d$. The standard tools for this process are B-splines and non-uniform rational B-splines (NURBS) [28]. Given a knot vector $\Xi = \{\xi_1, \dots, \xi_{n+p+1}\} \subset [0, 1]$ such that $\xi_1 \leq \xi_2 \leq \dots \leq \xi_{n+p+1}$, a basis of n univariate B-splines of degree p can be defined using the Cox-de-Boor recursion formula

$$B_i^p(\xi) = \frac{\xi - \xi_i}{\xi_{i+p} - \xi_i} B_i^{p-1}(\xi) + \frac{\xi_{i+p+1} - \xi}{\xi_{i+p+1} - \xi_{i+1}} B_{i+1}^{p-1}(\xi), \quad i = 1, \dots, n, \quad (1a)$$

$$B_i^0(\xi) = \begin{cases} 1, & \xi_1 \leq \xi < \xi_{i+1}, \\ 0, & \text{otherwise.} \end{cases} \quad (1b)$$

Univariate NURBS basis functions are defined as

$$N_i^p(\xi) = \frac{w_i B_i^p(\xi)}{\sum_{j=1}^n w_j B_j^p(\xi)}, \quad (2)$$

where w_i are positive weights. Using n NURBS basis functions along with n control points $\{\mathbf{P}_i\}_{i=1}^n \subset \Omega$, a NURBS curve can be defined as

$$\mathbf{C}(\xi) = \sum_{i=1}^n \mathbf{P}_i N_i^p(\xi). \quad (3)$$

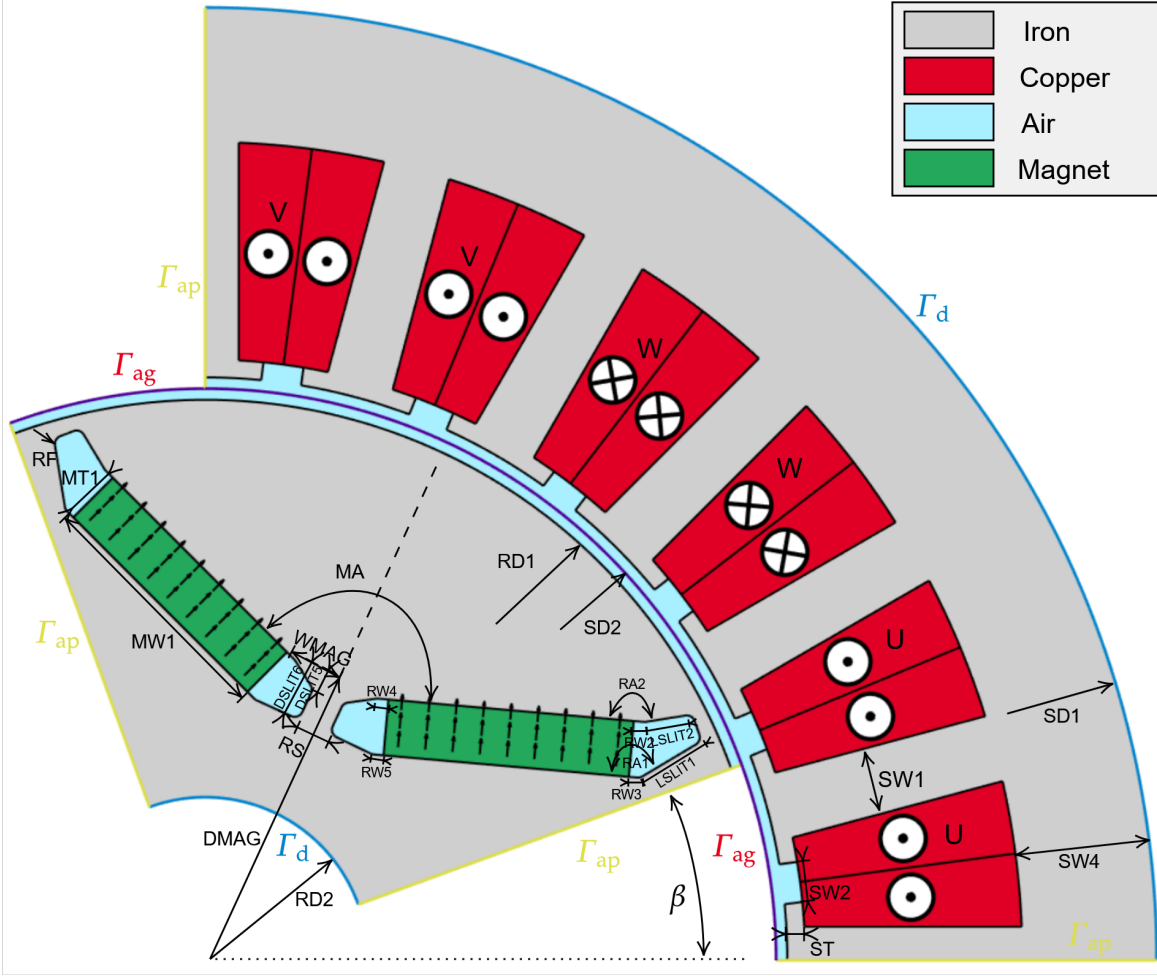


Figure 1: One-fourth of the PMSM's geometry in two dimensions, including material distribution, boundary conditions, and geometric design parameters (see Table 1). The phase and current direction in the copper coils is also shown. Figure adapted from [21].

NURBS surfaces or higher-dimensional objects can be created using tensor products of NURBS curves. Using these constructions, it is possible to define a map $F : [0, 1]^d \rightarrow \Omega$ that parametrizes the physical domain such that $\mathbf{x} = F(\boldsymbol{\xi})$, $\mathbf{x} \in \Omega$, $\boldsymbol{\xi} \in [0, 1]^d$.

Not that, in most practical applications, the geometry cannot be parametrized using a single projection map from the reference to the physical domain. This is also the case for the considered PMSM, which features a complex geometry with different material subdomains. In such cases, a multi-patch parametrization is used, where the physical domain is decomposed into a collection of subdomains, each with a corresponding projection map, to be appropriately combined [29].

2.2 Magnetostatic model

The magnetic field distribution on the PMSM is obtained by the magnetostatic formulation, which for a magnetic vector potential \mathbf{A} reads

$$\nabla \times (\nu \nabla \times \mathbf{A}) = \mathbf{J}_{\text{src}} + \nabla \times (\nu \mathbf{B}_r), \quad (4)$$

where $\mathbf{B} = \nabla \times \mathbf{A}$ denotes the magnetic flux density, $\nu = \nu(|\mathbf{B}|)$ the (nonlinear) reluctivity, \mathbf{J}_{src} the source current density, and \mathbf{B}_r the remanent flux density of the permanent magnets. Note that this formulation neglects displacement and eddy currents, which is common practice for laminated PMSMs. Moreover,

assuming invariance along the z -axis and neglecting three-dimensional effects, e.g., due to end windings, the two-dimensional problem is considered, simplifying (4) to the Poisson problem

$$\nabla \cdot (\nu \nabla A_{z,\text{rt}}) = \nu \nabla \cdot \mathbf{B}_r, \quad \text{in } \Omega_{\text{rt}}, \quad (5a)$$

$$\nabla \cdot (\nu \nabla A_{z,\text{st}}) = -J_{z,\text{src}}, \quad \text{in } \Omega_{\text{st}}, \quad (5b)$$

where Ω_{rt} and Ω_{st} denote the rotor and stator domains, respectively. Note that (5) requires only the z -components of the magnetic vector potential and the source current density, i.e., $\mathbf{A} = (0, 0, A_z)$ and $\mathbf{J}_{\text{src}} = (0, 0, J_{z,\text{src}})$. Problem (5) is complemented with homogeneous Dirichlet and anti-periodic boundary conditions, respectively applied to the boundaries denoted with Γ_{d} and Γ_{ap} in Figure 1. Additionally, field continuity at the air gap interface Γ_{ag} is ensured by the coupling conditions

$$A_{z,\text{st}}(\theta) = A_{z,\text{rt}}(\theta - \beta), \quad \text{on } \Gamma_{\text{ag}}, \quad (6a)$$

$$H_{\theta,\text{st}}(\theta) = H_{\theta,\text{rt}}(\theta - \beta), \quad \text{on } \Gamma_{\text{ag}}, \quad (6b)$$

where $\mathbf{H} = \nu \mathbf{B}$ is the magnetic field strength and A_z, H_θ are evaluated in local, rotor- or stator-specific coordinate systems that depend on the rotation angle β [30]. The remanent flux density \mathbf{B}_r is given as $\mathbf{B}_r = B_r (-\sin(\alpha), \cos(\alpha))$, where α is the magnets' direction angle. Last, the source current density is given as $J_{z,\text{src}} = \sum_k J_{z,\text{src}}^{(k)}$, $k \in \{1, 2, 3\}$, and the k -th phase current is given as

$$J_{z,\text{src}}^{(k)} = J_0 \sin \left(n_{\text{pp}} \beta + \phi_0 + \frac{2\pi}{3} k \right), \quad (7)$$

where the magnitude J_0 depends on the application current and the coils' characteristics, ϕ_0 is the electric phase offset, and n_{pp} the number of pole pairs. A uniform distribution of $J_{z,\text{src}}$ within the coils is assumed.

2.3 Numerical approximation

The IGA method is used to solve problem (5) numerically, such that the basis functions of the CAD geometry representation are also used as basis functions for the numerical approximation of the solution [22]. Additionally, using harmonic mortaring for rotor-stator coupling [31] results in the matrix system

$$\underbrace{\begin{pmatrix} \mathbf{K}_{\text{rt}} & \mathbf{0} & -\mathbf{G}_{\text{rt}} \\ \mathbf{0} & \mathbf{K}_{\text{st}} & \mathbf{G}_{\text{st}} \mathbf{R}_\beta \\ -\mathbf{G}_{\text{rt}}^\top & \mathbf{R}_\beta^\top \mathbf{G}_{\text{st}}^\top & \mathbf{0} \end{pmatrix}}_{=\mathbf{K}} \underbrace{\begin{pmatrix} \mathbf{u}_{\text{rt}} \\ \mathbf{u}_{\text{st}} \\ \boldsymbol{\lambda} \end{pmatrix}}_{=\mathbf{u}} = \underbrace{\begin{pmatrix} \mathbf{b}_{\text{rt}} \\ \mathbf{b}_{\text{st}} \\ \mathbf{0} \end{pmatrix}}_{=\mathbf{b}}, \quad (8)$$

where $\mathbf{K}_{\text{rt}}, \mathbf{K}_{\text{st}}$ are stiffness matrices and $\mathbf{G}_{\text{rt}}, \mathbf{G}_{\text{st}}$ coupling matrices for the rotor and stator, respectively, \mathbf{R}_β is the rotation matrix for a given rotation angle β , $\boldsymbol{\lambda}$ is the vector of Lagrange multipliers, and $\mathbf{b}_{\text{rt}}, \mathbf{b}_{\text{st}}$ are the rotor- and stator-specific right-hand side vectors. For more details on constructing the matrix system (8) the reader is referred to [21]. Note that the system matrix \mathbf{K} actually depends on the solution vector \mathbf{u} due to the nonlinear constitutive law. Based on energy conservation principles [30], the electromagnetic torque, denoted as τ_β for a given rotation angle β , is computed as

$$\tau_\beta(\mathbf{u}) = -\mathbf{u}_{\text{st}}^\top \mathbf{G}_{\text{st}} \frac{d\mathbf{R}_\beta}{d\beta} \boldsymbol{\lambda} L, \quad (9)$$

where L is the axial length of the PMSM. The latter must be explicitly taken into account since the numerical solution corresponds to the two-dimensional problem.

2.4 PMSM model parameters and design variations

Following Wiesheu et al. [21], a PMSM model with the standard M330-50A material is utilised. The equivalent M27 data from the FEMM software [32] are used to define the nonlinear relative permeability, i.e., the inverse of the magnetic reluctivity (see section 2.2) of the iron parts. Nd-Fe-B (linear) magnets with remanence $B_r = 1.0$ T and relative permeability $\mu_r = 1.05$ are used. The PMSM operates with an applied current $I_{\text{app}} = 3$ A and its coils have $n_{\text{wind}} = 35$ windings. The IGA discretization of the PMSM’s geometry utilises 32 patches with 444 control points for the rotor domain and 144 patches with 365 control points for the stator domain. The geometry of the PMSM depends on $P = 20$ design parameters, which are shown in Figure 1 and listed in Table 1. These parameters take values within predefined ranges, also listed in Table 1. The different geometric design configurations arising from the possible parameter combinations have a significant impact on the computational domain of the PMSM model, its numerical solution, and finally on QoIs estimated by post-processing the solutions, such as the electromagnetic torque. The latter is the main QoI in this work. Collecting all geometric design parameters in a vector $\mathbf{p} \in \mathbb{R}^P$, system (8) becomes parameter-dependent with system matrix $\mathbf{K} = \mathbf{K}(\mathbf{p})$, right-hand side $\mathbf{b} = \mathbf{b}(\mathbf{p})$, and solution $\mathbf{u} = \mathbf{u}(\mathbf{p})$. Accordingly, the electromagnetic torque is parameter-dependent as well. We write, by abuse of notation, $\tau_\beta(\mathbf{u}) = \tau_\beta(\mathbf{u}(\mathbf{p})) = \tau_\beta(\mathbf{p})$.

To illustrate the impact of geometric design variations upon the torque of the PMSM, Figure 2 shows samples of torque signals, each corresponding to a different set of design parameter values. Note that the torque repeats every 30° of rotation due to the symmetry in the stator’s winding pattern. As can be observed, geometric design variations lead to significant changes in the torque signal. Also note that generating the torque signal for each geometric design variation entails running a computationally expensive numerical simulation for the solution of problem (5). A computationally inexpensive estimation of the torque would be preferable, especially considering UQ [33–36] or related studies like robust or reliability-based optimization [37–39], that necessitate repetitive and possibly numerous model evaluations for varying PMSM designs.

Table 1: Geometric design parameters of the PMSM and their value ranges. The lower and upper bounds of the parameter values are given in mm.

#	Geometric parameter	Lower bound	Upper bound
1	LSLIT1	6.1	6.7
2	LSLIT2	4.1	4.5
3	DSLIT5	0.9	1.1
4	DSLIT6	1.9	2.1
5	MA	142.5	157.5
6	MT1	3.8	4.2
7	MW1	20.9	23.1
8	RA1	136.8	151.2
9	RA2	157.7	174.3
10	RS	0.9	1.1
11	RW2	0.9	1.1
12	RW3	0.9	1.1
13	RW4	0.9	1.1
14	RW5	0.9	1.1
15	WMAG	3.8	4.2
16	DMAG	28.5	31.5
17	ST	1.5	1.7
18	SW1	5.7	6.3
19	SW2	3.4	3.8
20	SW4	24.2	26.8

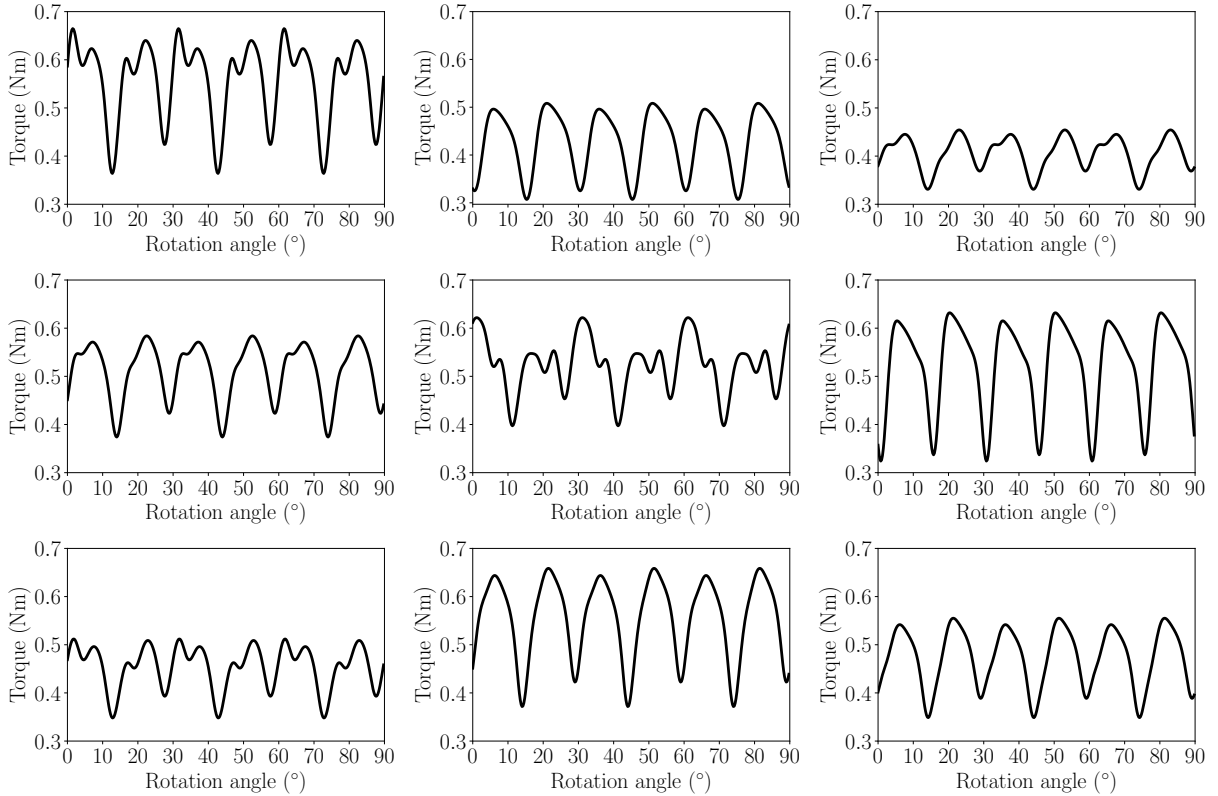


Figure 2: Torque signals for different geometric design configurations of the PMSM.

3. Reduced-order surrogate modeling framework

To address the need for computationally inexpensive torque estimates given different design configurations of the PMSM, we propose a data-driven framework for computing a surrogate model that can reliably replace the original, high-fidelity model in parameter studies such as UQ. The framework consists of a reduced-order modeling part and an inference part.

The reduced-order modeling part of the framework consists of the following steps:

0. *Data acquisition:* We assume that a dataset $\mathcal{D} = \{\mathbf{p}^{(m)}, \boldsymbol{\tau}^{(m)} = \boldsymbol{\tau}(\mathbf{p}^{(m)})\}_{m=1}^M$ is made available, containing different parameter realizations $\mathbf{p}^{(m)} \in \mathbb{R}^P$ and the corresponding torque signals $\boldsymbol{\tau}^{(m)} \in \mathbb{R}^N$, where N is the signal's dimension, defined by the number of rotation angles β_n for which the corresponding torque values τ_{β_n} are obtained, such that $\boldsymbol{\tau}^{(m)} = \left\{ \tau_{\beta_n}^{(m)} \right\}_{n=0}^{N-1}$. Continuous torque signals, e.g., as in Figure 2, are obtained by means of linear interpolation. In this work, such a dataset is obtained by evaluating the PMSM's numerical model for different design configurations. However, it is possible to use experimental data as well.
1. *Dimension reduction of the QoI:* The torque signals $\boldsymbol{\tau}^{(m)}$, $m = 1, \dots, M$, are processed such that the original dimension of the QoI is significantly reduced. In this work, dimension reduction is performed by applying DFT upon the torque signals and retaining the most important frequency components. Essentially, the dimension reduction step creates a map $\mathcal{R}: \boldsymbol{\tau} \rightarrow \mathbf{r}$, where \mathbf{r} denotes the reduced QoI, equivalently, the representation of the original QoI in a reduced frequency space.
2. *ML regression:* RSMS are trained by means of ML regression, as to map the design parameters to the reduced frequency components of the torque signals. We denote this map as $\mathcal{S}: \mathbf{p} \rightarrow \mathbf{r}$. Three RSMS are employed for that purpose, namely, PCE, FNN, and GP.

The inference part of the framework consists of the following steps:

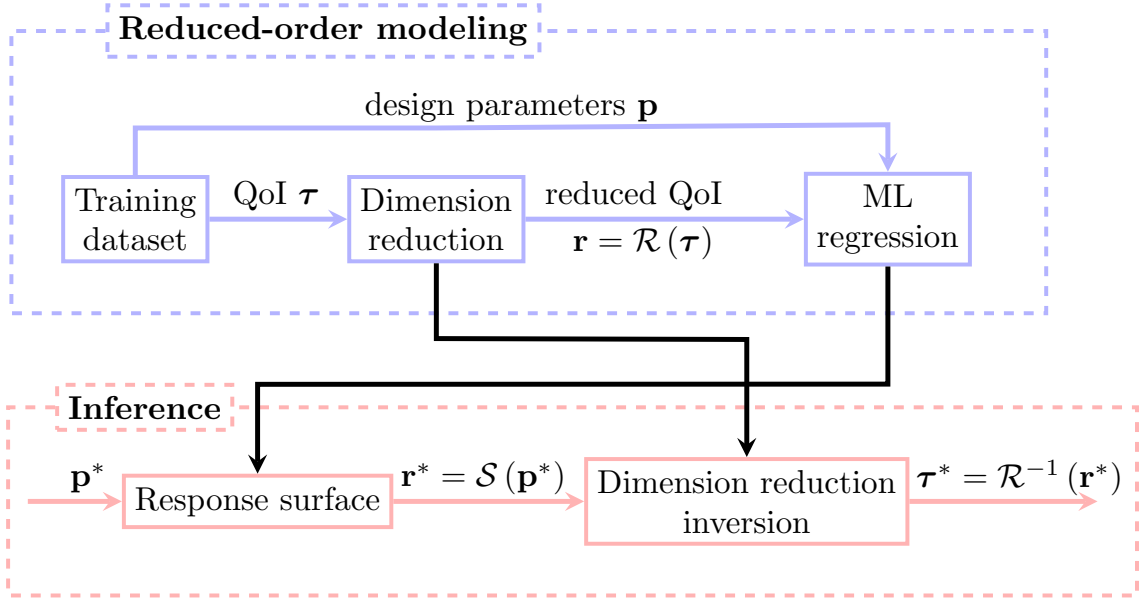


Figure 3: Schematic illustration of the surrogate modeling framework, separated into reduced-order modeling and inference parts.

1. *Response surface evaluation:* Given a new design configuration and the corresponding design parameter vector \mathbf{p}^* , the RSM is evaluated as to yield an estimate of the reduced QoI, such that $\mathbf{r}^* = \mathcal{S}(\mathbf{p}^*)$.
2. *Dimension reduction inversion:* The torque estimate for the new design configuration is obtained by inverting the dimension reduction procedure used in the reduced-order modeling part, such that $\tau^* = \mathcal{R}^{-1}(\mathbf{r}^*)$.

A visualization of the complete framework is provided in Figure 3. For UQ purposes, the resulting surrogate model can replace the high-fidelity model within a Monte Carlo sampling algorithm to obtain estimates of the torque's statistics (e.g., expected value, variance) cost-effectively. Details regarding the DFT-based dimension reduction approach are given in section 3.1. The computation of RSMs by means of ML regression is presented in section 3.2.

Remark on computational cost The computational cost of the suggested surrogate modeling framework concerns mainly the reduced-order modeling part, in particular data acquisition and ML regression. In this work, data acquisition is the main computational cost to be considered, since datasets are generated by running computationally expensive numerical model evaluations. In other cases, e.g., for datasets that are readily available, this cost can be insignificant. ML regression costs may range from negligible to quite significant, depending on choices regarding the type of ML model, training/optimization algorithm, and size of training dataset. Additionally, UQ costs must be considered, which mainly refer to sampling the model as part of a Monte Carlo algorithm. Assuming that the surrogate model is sampled, this cost is significantly reduced compared to sampling the original, high-fidelity model. Overall, in this work, the cost of data acquisition dominates, while ML regression and UQ costs can be neglected.

3.1 Dimension reduction via discrete Fourier transform

In the following, we assume that M torque signals $\tau^{(m)}$, $m = 1, \dots, M$, are available, consisting of N torque values within one rotation period. Longer torque signals can always be reduced to a single period without loss of information. Due to the fact that the dimensionality of the torque signal can be

prohibitively large for the subsequent steps of the surrogate modeling framework, we suggest an approach based on the DFT to reduce the torque's dimension to its minimum necessary frequency components.

The DFT is first used to convert a finite sequence of equally-spaced torque samples (in time, equivalently, with respect to rotation angle) into a sequence of the same length, where the latter contains information about the underlying frequency components that contribute to the given torque signal. Given the torque signal as a sequence of torque values per rotation angle, i.e., $\boldsymbol{\tau}^{(m)} = \{\tau_{\beta_n}^{(m)}\}_{n=0}^{N-1}$, the DFT yields the sequence of complex values $\mathbf{c}^{(m)} = \{c_k^{(m)}\}_{k=0}^{N-1}$, such that

$$c_k^{(m)} = \sum_{n=0}^{N-1} \tau_{\beta_n}^{(m)} \exp\left(-\frac{i2\pi kn}{N}\right) = \sum_{n=0}^{N-1} \tau_{\beta_n}^{(m)} \left(\cos\left(-\frac{2\pi kn}{N}\right) - i \sin\left(-\frac{2\pi kn}{N}\right) \right), \quad (10)$$

where $c_0^{(m)} \in \mathbb{R}$ corresponds to the average value of the original torque signal $\boldsymbol{\tau}^{(m)}$ across all rotation-angle samples. Since the torque signal is real-valued, its average value is real-valued as well. The DFT can be inverted to reconstruct the original signal, such that

$$\tau_{\beta_n}^{(m)} = \frac{1}{N} \sum_{k=0}^{N-1} c_k^{(m)} \exp\left(-\frac{i2\pi kn}{N}\right). \quad (11)$$

For the purpose of dimension reduction, we take advantage of the fact that the power spectrum of a given torque signal $\boldsymbol{\tau}^{(m)}$ can be given in terms of its frequency components as

$$\text{PS}_k^{(m)} = \frac{1}{N} |c_k^{(m)}|^2, \quad (12)$$

meaning that each frequency component has a distinct contribution to the power spectrum, quantified by the value $\eta_k = |c_k^{(m)}|^2$. Omitting components with negligible contributions to the power spectrum allows to reduce the dimensionality of the output of the DFT without significantly affecting the value of the power spectrum, but also without compromising the accuracy of the torque's reconstruction given in (11) due to the small values of the omitted constants $c_k^{(m)}$.

However, for varying design configurations, each corresponding to a different torque signal, it is to be expected that the DFT output will differ from one signal to another. In turn, the classification of frequency components to negligible or retainable shall differ among the torque signals. To address this issue, we suggest to retain the frequency components that remain important over the possible design configurations in the sense of expected contribution to the power spectrum. To that end, the contribution of each frequency component to the power spectrum over all given torque signals $\boldsymbol{\tau}^{(m)}$, $m = 1, \dots, M$, is averaged as to obtain a single contribution per component, computed as

$$\bar{\eta}_k = \frac{1}{M} \sum_{m=1}^M \eta_k = \frac{1}{M} \sum_{m=1}^M |c_k^{(m)}|^2. \quad (13)$$

Subsequently, the frequency components are sorted based on their averaged power spectrum contributions. The dimension reduction of the DFT's output proceeds by keeping the frequency components corresponding to non-negligible averaged power spectrum contributions $\bar{\eta}_k$, accordingly neglecting frequency components with negligible averaged contributions.

This procedure results in a reduced QoI $\mathbf{r} \in \mathbb{C}^R$, $R < N$, with $\mathbf{r} = \{c_{k'}\}_{k' \in \mathcal{I}}$, where $\mathcal{I} \subset \{k\}_{k=0}^{N-1}$ is an index set with cardinality equal to R that contains the indices of the retained frequency components. Put in a ROM context, $\mathbf{r} \in \mathbb{C}^R$ is the reduced representation (here, in frequency space) of $\boldsymbol{\tau} \in \mathbb{R}^N$ and $\{c_{k'}\}_{k' \in \mathcal{I}}$ is the corresponding reduced basis. Accordingly, the realizations of the reduced QoI are given as $\mathbf{r}^{(m)} = \{c_{k'}^{(m)}\}_{k' \in \mathcal{I}}$, $m = 1, \dots, M$. Note that the reduced QoI can be given equivalently as a real vector $\mathbf{r} \in \mathbb{R}^{2R-1}$, by considering separately the real and imaginary parts of the complex elements $c_{k'}$,

$k' \neq 0$, where $c_0 \in \mathbb{R}$. We opt for the more concise complex notation.

3.2 Regression-based response surface models

Within the suggested surrogate modeling framework, data-driven, regression-based RSMs are employed to approximate the functional relationship between the geometric parameters of the PMSM and the reduced frequency components of the torque signal, thus providing a map $\mathcal{S} : \mathbf{p} \rightarrow \mathbf{r}$. For comparison purposes, in the numerical experiments presented in section 4, the RSMs are employed as approximations to full torque signals and to their reduced principal components. Therefore, in the following, the functional relation is denoted as $\mathbf{y} = f(\mathbf{p})$, where \mathbf{y} may refer to either the full or reduced QoI. Without loss of generality, we assume that $\mathbf{y} \in \mathbb{R}^N$. For the regression-based computation of the RSMs, we assume the existence of a dataset $\mathcal{D}_t = \{\mathbf{p}^{(m)}, \mathbf{y}^{(m)}\}_{m=1}^M$ containing input parameter realizations along with the corresponding values of the QoI. Three RSMs are examined, namely, PCE, FNN, and GP, which are briefly presented next.

3.2.1 Polynomial chaos expansion (PCE)

For response surface modeling by means of the PCE, the parameter vector \mathbf{p} is assumed to be a random vector defined on the probability space $(\Theta, \Sigma, \mathcal{P})$, where Θ denotes the sample space, Σ the sigma algebra of events, and $\mathcal{P} : \Sigma \rightarrow [0, 1]$ a probability measure, and with the probability density function (PDF) $\varrho(\mathbf{p}) : \Xi \rightarrow \mathbb{R}_{\geq 0}$, where $\Xi \subset \mathbb{R}^P$ denotes the random vector's support. Under these assumptions, a PCE is a global polynomial approximation of the form

$$f(\mathbf{p}) \approx f_{\text{PCE}}(\mathbf{p}) = \sum_{k=1}^K \mathbf{a}_k \Psi_k(\mathbf{p}), \quad (14)$$

where $\mathbf{a}_k \in \mathbb{R}^N$ are expansion coefficients and Ψ_k are multivariate polynomials that satisfy the orthogonality property

$$\mathbb{E}[\Psi_k \Psi_l] = \int_{\Xi} \Psi_k(\mathbf{p}) \Psi_l(\mathbf{p}) \varrho(\mathbf{p}) d\mathbf{p} = \mathbb{E}[\Psi_k^2] \delta_{kl}, \quad (15)$$

where δ_{kl} is the Kronecker delta. Depending on the PDF, the polynomials are chosen either according to the Wiener-Askey scheme [40] or are constructed numerically [41]. The polynomial basis of the PCE can be formed in several ways, which also define the truncation limit K . Common options include total degree, hyperbolic truncation, sparse, and adaptive bases, and combinations thereof [42].

Training the PCE means fitting its coefficients based on the data \mathcal{D}_t . In particular, the coefficients are computed by solving the least squares regression problem

$$\arg \min_{\mathbf{a}_1, \dots, \mathbf{a}_K} \left\{ \frac{1}{M} \sum_{m=1}^M \left(\mathbf{y}^{(m)} - \sum_{k=1}^K \mathbf{a}_k \Psi_k(\mathbf{p}^{(m)}) \right)^2 \right\}. \quad (16)$$

For sparse PCEs, the regression problem (16) is complemented with an additional penalty term that induces sparsity in its solution. In this work, we opt for a sparse and adaptive PCE method based on least angle regression (LAR) [43], which is implemented with the UQLab software [44].

3.2.2 Feedforward neural network (FNN)

To define an FNN, we must first introduce the concepts of neuron and layer. A neuron is the smallest unit of an FNN and is mathematically described by the function

$$\nu(\mathbf{z}) = \sigma(\mathbf{z}^\top \mathbf{w} + b), \quad (17)$$

where $\mathbf{z} \in \mathbb{R}^D$ is the input to the neuron, $\mathbf{w} \in \mathbb{R}^D$ a weight vector, $b \in \mathbb{R}$ a bias term, and $\sigma : \mathbb{R} \rightarrow \mathbb{R}$ a nonlinear function commonly referred to as the activation. A layer is formed by a set of K neurons that receive the same input $\mathbf{z} \in \mathbb{R}^D$ and is mathematically described by the function

$$\ell(\mathbf{z}) = \sigma(\mathbf{z}^\top \mathbf{W} + \mathbf{b}), \quad (18)$$

where $\mathbf{W} \in \mathbb{R}^{D \times K}$ is a matrix that contains the weights of the K neurons in the layer, $\mathbf{b} \in \mathbb{R}^K$ is the corresponding bias vector, and the activation function is applied elementwise per neuron. The FNN is formed as a sequence of L layers and is mathematically described by the layer composition formula

$$f_{\text{FNN}}(\mathbf{z}) = \ell^L(\ell^{L-1}(\dots(\ell^1(\mathbf{z}))))). \quad (19)$$

To be used as an RSM $f_{\text{FNN}}(\mathbf{p}) \approx f(\mathbf{p})$, the FNN's trainable parameters, i.e., the collection of its weights and biases $\boldsymbol{\theta} = \{\mathbf{W}^{(l)}, \mathbf{b}^{(l)}\}_{l=1}^L$ must be fitted to the training data \mathcal{D}_t . Here, this is accomplished by minimizing the mean square error (MSE) loss function

$$\mathcal{L}(\boldsymbol{\theta}) = \frac{1}{M} \sum_{m=1}^M \left(\mathbf{y}^{(m)} - f_{\text{FNN}}(\boldsymbol{\theta}; \mathbf{p}^{(m)}) \right)^2, \quad (20)$$

resulting in a nonlinear optimization problem, the solution of which is typically computed by means of stochastic gradient descent algorithms [45] enabled by automatic differentiation [46].

In this work we opt for an FNN consisting of four fully-connected hidden layers with 45, 60, 80, and 25 neurons, respectively. Naturally, the number of neurons used in the output layer coincide with the dimensions of the QoI (original or reduced). Rectified linear unit (ReLU) activation functions are used for all neurons. The FNN is trained for 600 epochs using a standard stochastic gradient descent optimizer with scheduled learning rate. The `Tensorflow` software [47] is used for implementation.

3.2.3 Gaussian process (GP)

A GP is formally defined as a collection of random variables, any finite number of which have a joint Gaussian distribution [48]. Considering temporarily a scalar QoI $y = f(\mathbf{p})$, an approximation by a GP interprets the functional relation as a probability distribution in function space, such that

$$f(\mathbf{p}) \sim \mathcal{GP}(m(\mathbf{p}), k(\mathbf{p}, \mathbf{p}')), \quad (21)$$

where $m(\mathbf{p})$ is a mean function and $k(\mathbf{p}, \mathbf{p}')$ a covariance function. The mean and covariance functions encode prior assumptions regarding the target function, e.g., concerning its expected behavior and regularity. The prior assumptions are then combined with the data available in the training dataset \mathcal{D}_t as to obtain a new GP, called the posterior, with updated mean and covariance functions. Defining the matrix $\mathbf{K} \in \mathbb{R}^{M \times M}$ with elements $k_{ij} = k(\mathbf{p}^{(i)}, \mathbf{p}^{(j)})$, and the vector $\mathbf{m} = (m(\mathbf{p}^{(1)}), \dots, m(\mathbf{p}^{(M)})) \in \mathbb{R}^M$, the updated (posterior) distribution of the target function, i.e., conditioned on the training dataset \mathcal{D}_t , is given as

$$f(\mathbf{p})|\mathcal{D}_t \sim \mathcal{N}(\mathbf{m}, \mathbf{K}), \quad (22)$$

where $\mathcal{N}(\cdot, \cdot)$ denotes a Gaussian distribution. For a new data point $\mathbf{p}^* \notin \mathcal{D}_t$, the predictive distribution is given as

$$f(\mathbf{p})|\mathbf{p}^*, \mathcal{D}_t \sim \mathcal{N}\left(\underbrace{m(\mathbf{p}^*) + \mathbf{k}(\mathbf{p}^*, \mathbf{P}) \mathbf{K}^{-1} (\mathbf{y} - \mathbf{m})^\top}_{\text{mean}}, \underbrace{k(\mathbf{p}^*, \mathbf{p}^*) - \mathbf{k}(\mathbf{p}^*, \mathbf{P}) \mathbf{K}^{-1} \mathbf{k}(\mathbf{P}, \mathbf{p}^*)^\top}_{\text{variance}}\right), \quad (23)$$

where $\mathbf{P} = (\mathbf{p}^{(m)})_{m=1}^M$, $\mathbf{y} = (y^{(m)})_{m=1}^M$, $\mathbf{k}(\mathbf{p}^*, \mathbf{P}) = (k(\mathbf{p}^*, \mathbf{p}^{(m)}))_{m=1}^M$, and $\mathbf{k}(\mathbf{P}, \mathbf{p}^*) = (k(\mathbf{p}^{(m)}, \mathbf{p}^*))_{m=1}^M$. The predictions of the GP-based RSM are obtained by evaluating the mean function of the predictive distribution upon new data points, equivalently,

$$f(\mathbf{p}) \approx f_{\text{GP}}(\mathbf{p}) = m(\mathbf{p}) + \mathbf{k}(\mathbf{p}, \mathbf{P}) \mathbf{K}^{-1} (\mathbf{y} - \mathbf{m})^\top. \quad (24)$$

In this work, the assumed prior has zero mean and the ellipsoidal Gaussian covariance function

$$k(\mathbf{p}, \mathbf{x}' | \boldsymbol{\theta}) = \exp \left(-\frac{1}{2} \sum_{i=1}^P \left(\frac{x_i - x'_i}{\theta_i} \right)^2 \right), \quad (25)$$

where $\boldsymbol{\theta} = (\theta_i)_{i=1}^P$ is a vector of hyperparameters. Training the GP-based RSM entails optimizing the hyperparameters such that the likelihood of observing the data contained within the training dataset \mathcal{D}_t , denoted as $\mathcal{P}(\mathcal{D}_t, \boldsymbol{\theta})$, is maximized [48]. Here, this is accomplished with a covariance matrix adaptation evolution strategy (CMA-ES) optimizer [49]. Similar to the PCE, the implementation of the GP-based RSM is based on the UQLab software [44].

Note that the presentation above concentrated on a scalar QoI and its approximation by a GP. Multi-output GPs can be obtained in various ways, for example, using a so-called co-Kriging model or assuming a multi-output covariance [50]. In this work, we opt for the simplest solution of considering the elements of a vector-valued QoI to be independent and treating them separately, which was found to be sufficient.

4. Numerical studies and results

In the following, we assess several aspects of suggested reduced-order surrogate modeling framework, in particular concerning the dimension reduction achieved for the QoI, the performance of the resulting surrogates in terms of prediction accuracy, and the accuracy of statistics estimates when the surrogates are used for UQ. The corresponding numerical studies are presented in sections 4.1, 4.2, and 4.3, respectively.

4.1 Dimension reduction of the QoI

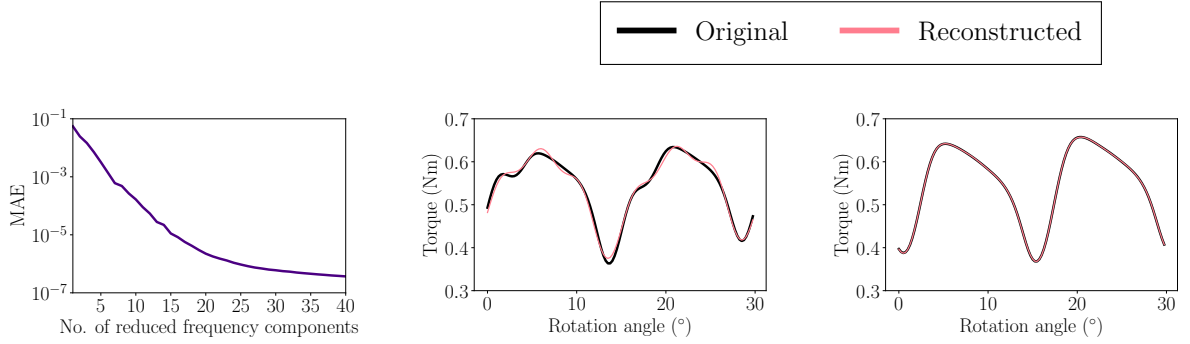
As previously explained in section 3.1, by keeping a reduced number of the frequency components obtained via DFT, the dimensions of the QoI can be reduced significantly. However, the number of reduced frequency components must be determined considering the trade-off between dimension reduction and the error between the reconstructed QoI, obtained by inverting the DFT, and the original. Therefore, in this first numerical study, we examine the optimal number of reduced QoI dimensions, such that torque signal reconstruction is sufficiently accurate compared to the original signals.

To identify the optimal level of dimension reduction, we first evaluate the mean absolute error (MAE)

$$\text{MAE} = \frac{1}{M} \sum_{m=1}^M \left\| \boldsymbol{\tau}^{(m)} - \mathcal{R}^{-1}(\mathbf{r}^{(m)}) \right\|_1, \quad (26)$$

where $\mathcal{R}: \boldsymbol{\tau} \in \mathbb{R}^N \rightarrow \mathbf{r} \in \mathbb{C}^R$, $R < N$, as discussed in section 3.1. To that end, we use a sample of $M = 2000$ torque signals, each containing $N = 120$ torque values τ_{β_n} evaluated at equidistantly distributed rotation angles $\beta_n \in [0^\circ, 30^\circ)$, $n = 0, \dots, N - 1$. It should be noted that if $R = N$, the original torque signal can be fully recovered without information loss, equivalently, the reconstruction error should be equal to zero (bearing machine accuracy). Figure 4a shows the relationship between reduced frequency components and the associated reconstruction error, which may provide an indication as to how many frequency components should be retained to achieve an average reconstruction accuracy.

However, the MAE is not informative concerning worst-case reconstruction errors. This can be verified by the results shown in Figure 4b, which shows the worst-case signal reconstruction for $R = 5$ frequency



(a) Reconstruction error versus reduced frequency components. (b) Worst-case reconstruction with $R = 5$ frequency components. (c) Worst-case reconstruction with $R = 11$ frequency components.

Figure 4: Reconstruction error versus dimension reduction and worst-case torque signal reconstructions using DFT-based dimension reduction with $R = 5$ and $R = 11$ reduced frequency components.

components. In this case, the MAE is equal to $3.2 \cdot 10^{-3}$, which should be sufficient for a reconstruction that is visually identical to the original signal, based on the torque values. Still, the reconstructed signal deviates significantly from the original, thus indicating that the retained frequency components are insufficient. The minimum number of frequency components to obtain a worst-case signal reconstruction that is visually identical to the original torque signal is $R = 11$, as can be observed in Figure 4c. In this case, the MAE equals $9.0 \cdot 10^{-5}$. Based on these observations and numerical results, in the following, $R = 11$ frequency components will be retained after the DFT.

4.2 Surrogate model accuracy

In this second numerical study, we assess the performance of surrogates obtained with the suggested framework in terms of prediction accuracy. Moreover, comparisons against alternative surrogates are performed, which use the same RSMs but either employ principal component analysis (PCA) [51] instead of DFT for dimension reduction or omit dimension reduction altogether. In the former case, 21 principal components are kept, resulting in an MAE equal to $2.8 \cdot 10^{-5}$ with respect to torque signal reconstruction. Note that the chosen number of principal components coincides with the number of reduced components obtained if the DFT-based, complex-valued, reduced QoI, $\mathbf{r} \in \mathbb{C}^R$, is transformed to an equivalent real-valued QoI, $\mathbf{r} \in \mathbb{R}^{2R-1}$, by considering separately the real and imaginary parts of the frequency components (see section 3.1), for $R = 11$ (see section 4.1).

For training and validation, an initial dataset $\mathcal{D} = \{\mathbf{p}^{(m)}, \boldsymbol{\tau}^{(m)} = \boldsymbol{\tau}(\mathbf{p}^{(m)})\}_{m=1}^M$, $M = 2000$, is partitioned into a training dataset \mathcal{D}_t and a validation dataset \mathcal{D}_v , where $\mathcal{D}_t \cap \mathcal{D}_v = \emptyset$. The training dataset size, M_t , is progressively increased such that $M_t \in \{600, 1200, 1800\}$, which allows to examine the effect of training data availability on surrogate modeling accuracy. Contrarily, the validation dataset remains fixed with size $M_v = 200$. Given a validation sample $(\mathbf{p}, \boldsymbol{\tau}) \in \mathcal{D}_v$, the absolute percentage error (APE) for a specific rotation angle β with corresponding torque value $\tau_\beta \in \boldsymbol{\tau}$ is computed as

$$\text{APE} = \frac{|\tau_\beta - \hat{\tau}_\beta|}{\tau_\beta}, \quad (27)$$

where $\hat{\tau}_\beta$ denotes the surrogate-based torque estimate. Aggregating the APE over the validation dataset, the error mean (MAPE) and standard deviation (SDAPE) can be computed, where the latter indicates the robustness of the surrogate with respect to its predictive accuracy. Doing the same for all rotation angles β_n , $n = 0, \dots, N - 1$, the MAPE and SDAPE are computed over a full signal period.

The MAPE and SDAPE results are shown in Figures 5 and 6, respectively, for all combinations of training dataset size, RSMs, and dimension reduction approach (or lack thereof). As would be expected, the accuracy and robustness of all surrogates is improved with more training data. The improvement

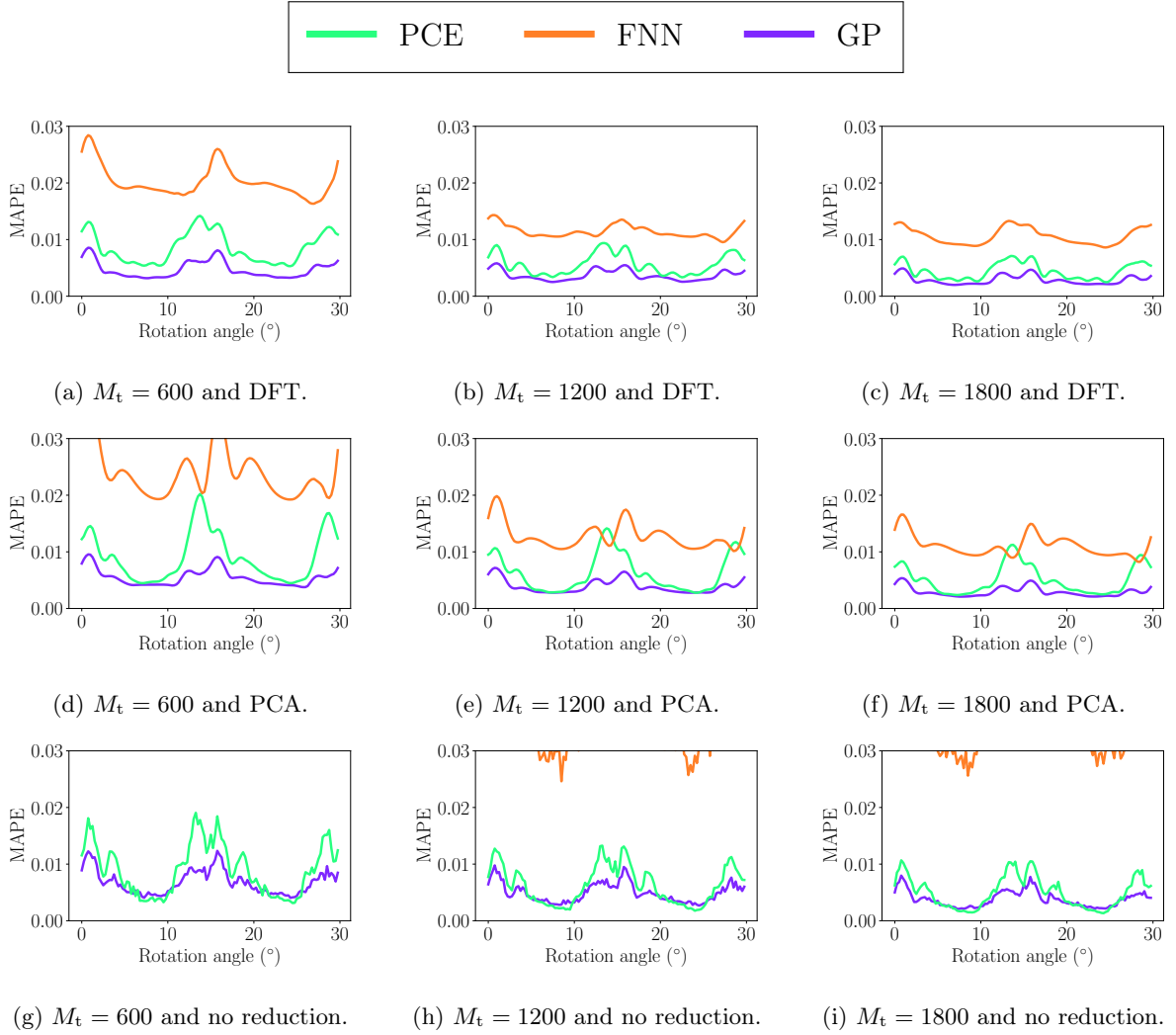


Figure 5: Mean absolute percentage error (MAPE) for surrogates computed with different combinations of training data size, RSM, and dimension reduction approach.

is significant when increasing the training dataset size from $M_t = 600$ to $M_t = 1200$, but only minor gains are obtained for a further increase to $M_t = 1800$. Irrespective of training dataset size or dimension reduction approach, GPs are generally the best RSM option in terms of surrogate modeling accuracy and robustness, especially if combined with dimension reduction. On the opposite side, FNN is consistently the worst-performing RSM option. Using DFT for dimension reduction yields overall more accurate and robust surrogates compared to PCA or no dimension reduction, especially given smaller training datasets. The combination of DFT-based dimension reduction with a GP-based RSM yields the best-in-class surrogate model. These observations are further supported by the results presented in Table 2, where the MAPE is averaged over the torque signal.

Table 2: Signal-averaged MAPE for surrogates computed with different combinations of training data size, RSM, and dimension reduction approach. The best-in-class error values for the same training dataset size are marked as bold.

M_t	DFT			PCA			No reduction		
	PCE	FNN	GP	PCE	FNN	GP	PCE	FNN	GP
600	0.0085	0.0203	0.0047	0.0091	0.02407	0.0055	0.0091	0.0526	0.0068
1200	0.0057	0.0114	0.0037	0.0063	0.0127	0.0039	0.0063	0.0379	0.0049
1800	0.0044	0.0106	0.0029	0.0051	0.0110	0.0030	0.0050	0.0371	0.0038

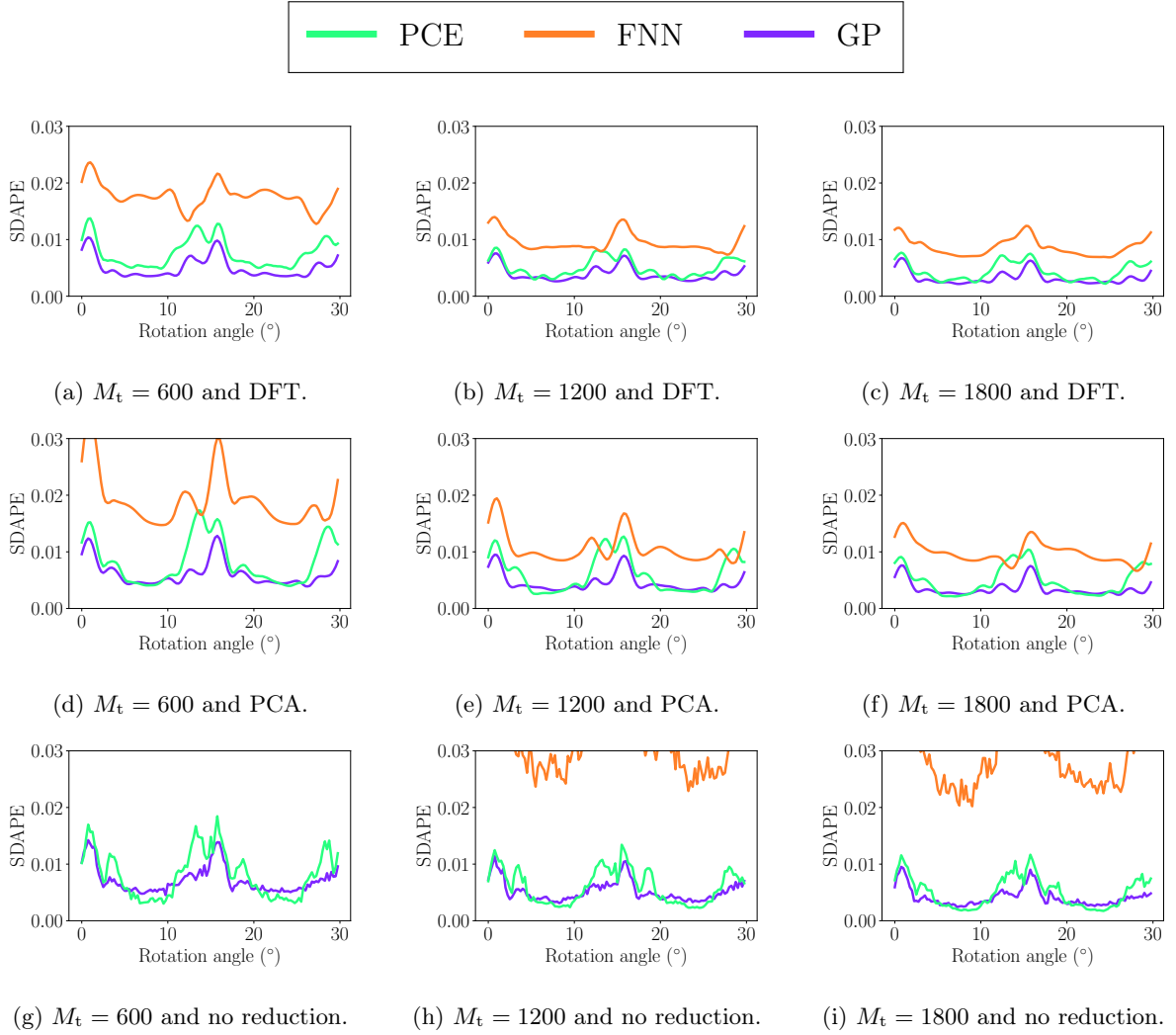


Figure 6: Standard deviation of absolute percentage error (SDAPE) for surrogates computed with different combinations of training data size, RSM, and dimension reduction approach.

Figure 7 shows the worst-case torque signal predictions for training dataset size $M_t = 1800$ and each combination of RSM and dimension reduction approach. The results for $M_t = 600$ and $M_t = 1200$ are available in the Appendix (Figures 9 and 10). In all cases, it is clear that surrogates based on FNNs perform much worse than PCE and GP-based ones. The latter two RSMs do not result in significant differences and only a slight edge can be claimed for GP. Note that, in the case of either DFT or PCA-based dimension reduction, the observed deviations between original and predicted torque signal can be attributed solely to training data availability and RSM approximation capability (see section 4.1).

Last but not least, it is worth noting that surrogate modeling accuracy and robustness clearly benefit from dimension reduction, both on average and in worst-case. This is particularly evident for the FNN, but actually applies to all RSMs. The enhancing effect of dimension reduction to the predictive accuracy of surrogate models is in fact known, e.g., considering deep operator learning in latent spaces [52]. It can be attributed to a filtering effect, where redundant features of the QoI that can potentially hinder its effective approximation are filtered out through dimension reduction. It is obvious both DFT and PCA provide this benefit, with a slight edge given to the former.

4.3 Surrogate-based uncertainty quantification

In this last numerical study, surrogates obtained with the suggested framework are used for UQ. In particular, they replace the original, high-fidelity model of the PMSM in Monte Carlo sampling, which

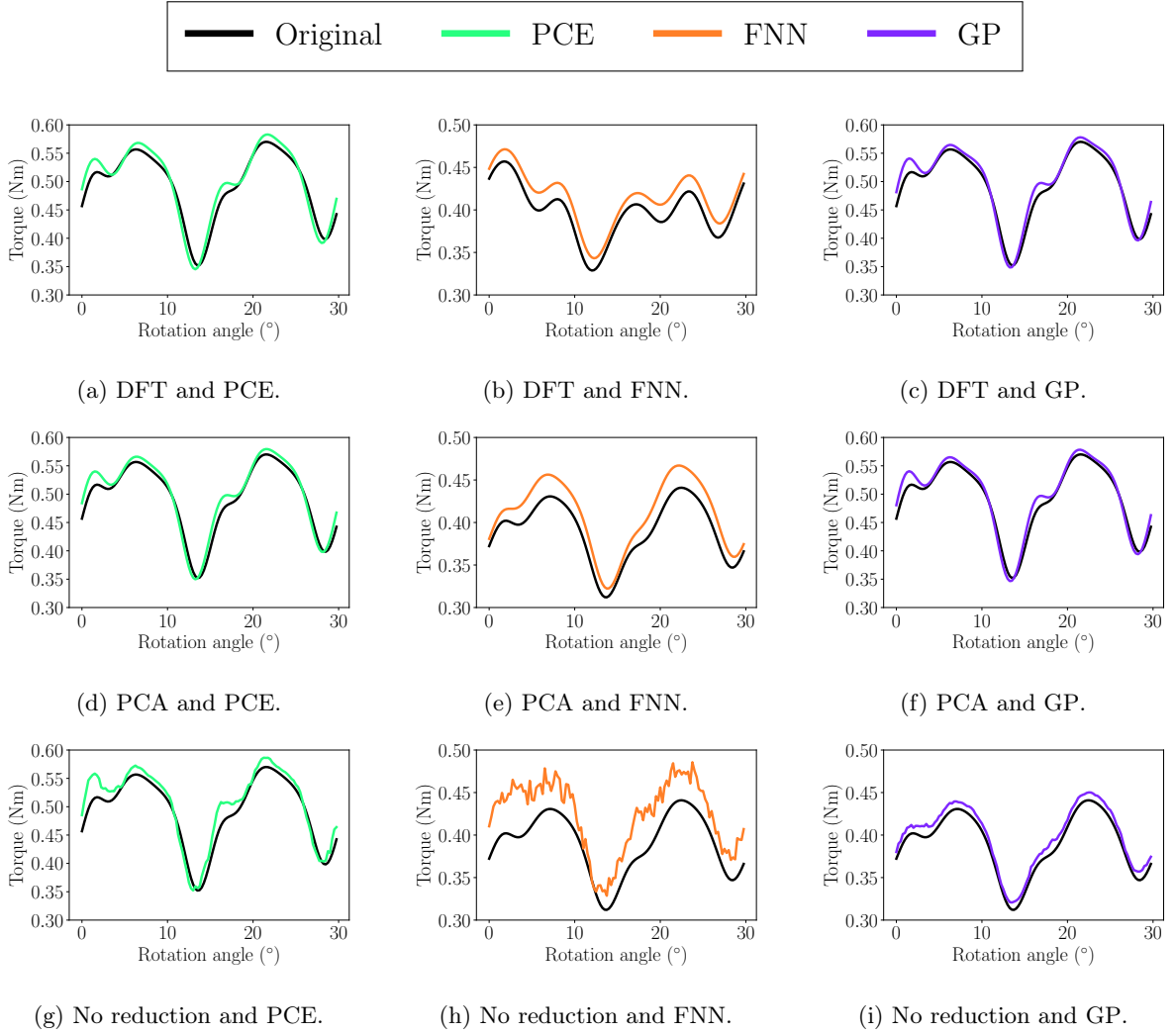


Figure 7: Worst-case surrogate-based torque signal predictions for training dataset size $M_t = 1800$ and different combinations of RSM and dimension reduction approach.

aims at estimating torque statistics, specifically mean values and standard deviations of torque signals. Additionally, surrogate-based estimates are compared against reference statistics obtained by sampling the original model. In either case, the model is sampled $11 \cdot 10^3$ times, where uniform distributions within the limits given in Table 1 are assumed for all design parameters. The sample mean and standard deviation of a torque value τ_β are denoted with $\hat{\mu}[\tau_\beta]$ and $\hat{\sigma}[\tau_\beta]$, respectively.

All surrogates provide estimates that visually overlap with the reference statistics, hence, the corresponding figures have been omitted as they hinder interpretation. Instead, Figure 8 shows the APE for the mean and standard deviation estimates relative to the reference statistics, for surrogates computed with different training dataset sizes and RSMs. In this section, all surrogates follow the suggested reduced-order surrogate modeling framework, therefore, DFT-based dimension reduction is exclusively used. With respect to mean estimates, it is observed that GP is consistently the best RSM option, followed by PCEs and FNNs, irrespective of training dataset size. This aligns with our findings in section 4.2 regarding surrogate modeling accuracy. In the case of standard deviation, however, no RSM choice consistently outperforms the others. One advantage of GP is the comparatively smaller error fluctuation. At the same time, FNNs and PCEs yield lower errors for large parts of the signal. This inconsistency could possibly be attributed to the reference standard deviation, which may not be sufficiently accurate for the given Monte Carlo sample size. Additionally, signal-averaged APEs per training dataset size and RSM are reported in Table 3. These results further confirm the observations above.

Last, we underline the computational gains achieved by using surrogate models for Monte Carlo-

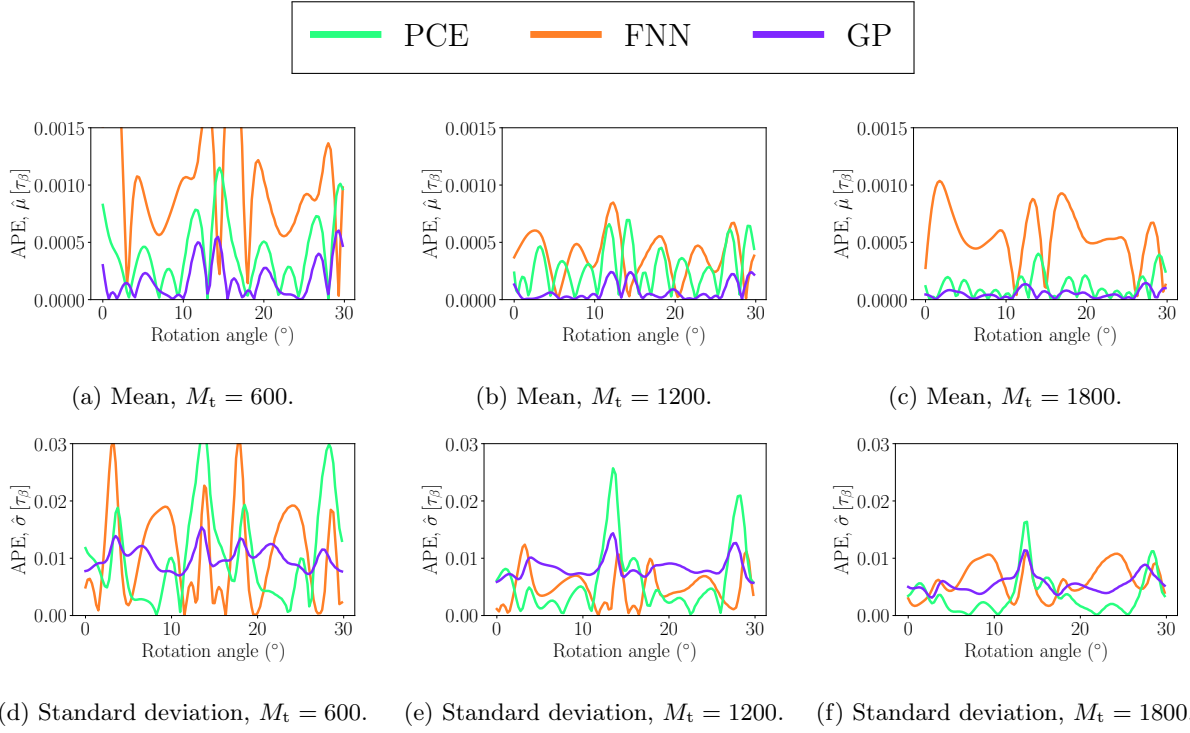


Figure 8: APE of torque mean and standard deviation estimates obtained with framework-based surrogates computed with different combinations of training dataset size and RSM.

based statistics estimates. Using an up-to-date CPU, a single high-fidelity PMSM model evaluation takes approximately 500 seconds. For the $11 \cdot 10^3$ random samples used for the Monte Carlo-based statistics estimates, this amounts to approximately 1528 CPU-hours. In contrast, generating training datasets with sizes $M_t \in \{600, 1200, 1800\}$ amounts to (approximately) 83, 167, and 250 CPU-hours, respectively. In this work, the cost due to training and sampling the surrogates can be regarded as negligible next to the data acquisition cost. Hence, depending on the training dataset size, the computational cost of the surrogate-based UQ study is $18\times - 6\times$ smaller than using the high-fidelity model, with statistics errors that can be considered more than acceptable. Note that the computational gains could possibly be much greater, for example, considering scenarios with smaller training datasets or larger Monte Carlo samples.

5. Conclusions

This work presented a novel, data-driven surrogate modeling framework, aiming at predicting the torque of a PMSM under geometrical design variations cost-effectively, and utilizing these predictions for cost-efficient UQ studies. The framework consists of a reduced-order modeling and an inference part. The reduced-order modeling part combines DFT-based dimension reduction of torque signals with regression-based RSMs that approximate the functional dependency between the PMSM's design parameters and

Table 3: Signal-averaged APE of surrogate-based mean and standard deviation estimates. The surrogates are computed using the suggested framework, for different training dataset sizes and RSMs. The best-in-class error values for the same training dataset size are marked as bold.

M_t	Mean			Standard Deviation		
	PCE	FNN	GP	PCE	FNN	GP
600	0.0004	0.0011	0.0002	0.0107	0.0110	0.0101
1200	0.0003	0.0004	0.0001	0.0061	0.0048	0.0083
1800	0.0001	0.0006	0.0001	0.0035	0.0062	0.0056

the reduced QoI. Three RSMs are tested, namely, PCE, FNN, and GP. In the inference part, the trained RSM is first evaluated for a set of new design parameters and subsequently an inverse DFT is applied to yield the predicted torque signal.

Our framework is applied for torque inference and UQ for a PMSM with 20 geometric design parameters. The torque signals contain 120 torque values evaluated upon equidistant rotation angles within a period. The numerical studies reveal a number of interesting observations. First, at least $R = 11$ frequency components must be kept in the ROM to ensure a sufficiently accurate torque signal reconstruction. Next, the best-in-class surrogate model in terms of prediction accuracy and robustness is obtained by combining DFT-based dimension reduction and GP-based RSM. This result includes comparisons against non-framework-based surrogate models, which either replace DFT with PCA in the dimension reduction step or omit it altogether. Importantly, omitting the dimension reduction step leads to severe deterioration in prediction accuracy. In surrogate-based UQ by means of Monte Carlo sampling, the GP remains the best RSM choice concerning mean torque estimation accuracy. However, for standard deviation estimation, no RSM can claim best performance. Last, surrogate-based UQ by means of Monte Carlo is several times more cost-efficient compared to sampling the high-fidelity PMSM model.

Overall, the suggested framework results in surrogate models that can reliably replace the high-fidelity PMSM model and enable otherwise computationally intractable parameter studies such as UQ, even outperforming commonly used approaches like direct QoI approximation or dimension reduction via PCA. The DFT-based dimension reduction is particularly suitable in this use case, given the physical characteristics of the QoI, mainly its periodicity. Periodicity is indeed present for a wide array of electric machine QoIs besides the torque. The method remains applicable for non-periodic QoIs as well, however, the extent of this applicability should be investigated further. Other extensions could consider a richer selection of RSM and dimension reduction possibilities, including nonlinear methods.

Acknowledgments The authors are partially supported by the joint DFG/FWF Collaborative Research Centre CREATOR (DFG: Project-ID 492661287/TRR 361; FWF: 10.55776/F90) at TU Darmstadt, TU Graz, and JKU Linz.

References

- [1] Steven Nadel. ‘Electrification in the transportation, buildings, and industrial sectors: a review of opportunities, barriers, and policies’. In: *Current Sustainable/Renewable Energy Reports* 6.4 (2019), pp. 158–168.
- [2] Gerd Bramerdorfer. ‘Effect of the manufacturing impact on the optimal electric machine design and performance’. In: *IEEE Transactions on Energy Conversion* 35.4 (2020), pp. 1935–1943.
- [3] Mikko I Jyrkama and Mahesh D Pandey. ‘On the separation of aleatory and epistemic uncertainties in probabilistic assessments’. In: *Nuclear Engineering and Design* 303 (2016), pp. 68–74.
- [4] Ralph C Smith. *Uncertainty Quantification: Theory, Implementation, and Applications*. SIAM, 2024.
- [5] Jiaxin Zhang. ‘Modern Monte Carlo methods for efficient uncertainty quantification and propagation: a survey’. In: *Wiley Interdisciplinary Reviews: Computational Statistics* 13.5 (2021), e1539.
- [6] Reza Alizadeh, Janet K Allen and Farrokh Mistree. ‘Managing computational complexity using surrogate models: a critical review’. In: *Research in Engineering Design* 31.3 (2020), pp. 275–298.
- [7] Jack P. C. Kleijnen. ‘Response Surface Methodology’. In: *Handbook of Simulation Optimization*. Ed. by Michael C Fu. New York, NY: Springer New York, 2015, pp. 81–104.

- [8] Serhat Hosder. ‘Stochastic response surfaces based on non-intrusive polynomial chaos for uncertainty quantification’. In: *International Journal of Mathematical Modelling and Numerical Optimisation* 3.1-2 (2012), pp. 117–139.
- [9] Utkarsh Thakre and Rakesh G Mote. ‘Uncertainty quantification and statistical modeling of selective laser sintering process using polynomial chaos based response surface method’. In: *Journal of Manufacturing Processes* 81 (2022), pp. 893–906.
- [10] Hossein Beheshti Nezhad, Mahmoud Miri and Mohammad Reza Ghasemi. ‘New neural network-based response surface method for reliability analysis of structures’. In: *Neural Computing and Applications* 31 (2019), pp. 777–791.
- [11] Zhaoyue Xu et al. ‘Artificial neural network based response surface for data-driven dimensional analysis’. In: *Journal of Computational Physics* 459 (2022), p. 111145.
- [12] Nuno Ricardo Costa and João Lourenço. ‘Gaussian process model – an exploratory study in the response surface methodology’. In: *Quality and Reliability Engineering International* 32.7 (2016), pp. 2367–2380.
- [13] Chuanhai Chen et al. ‘Modeling and prediction of spindle dynamic precision using the Kriging-based response surface method with a novel sampling strategy’. In: *Nonlinear Dynamics* 111.1 (2023), pp. 559–579.
- [14] Peter Benner, Serkan Gugercin and Karen Willcox. ‘A survey of projection-based model reduction methods for parametric dynamical systems’. In: *SIAM Review* 57.4 (2015), pp. 483–531.
- [15] Francisco Chinesta et al. ‘Model order reduction’. In: *Encyclopedia of Computational Mechanics* (2016), pp. 1–36.
- [16] Alessandro Alla and J Nathan Kutz. ‘Nonlinear model order reduction via dynamic mode decomposition’. In: *SIAM Journal on Scientific Computing* 39.5 (2017), B778–B796.
- [17] Anthony Nouy. ‘Low-Rank Tensor Methods for Model Order Reduction’. In: *Handbook of Uncertainty Quantification*. Ed. by Roger Ghanem, David Higdon and Houman Owhadi. Cham: Springer International Publishing, 2017, pp. 857–882.
- [18] Ludovica Cicci et al. ‘Uncertainty quantification for nonlinear solid mechanics using reduced order models with Gaussian process regression’. In: *Computers & Mathematics with Applications* 149 (2023), pp. 1–23.
- [19] George I Drakoulas et al. ‘FastSVD-ML-ROM: A reduced-order modeling framework based on machine learning for real-time applications’. In: *Computer Methods in Applied Mechanics and Engineering* 414 (2023), p. 116155.
- [20] Paolo Conti et al. ‘Multi-fidelity reduced-order surrogate modelling’. In: *Proceedings of the Royal Society A* 480.2283 (2024), p. 20230655.
- [21] Michael Wiesheu et al. ‘Combined parameter and shape optimization of electric machines with isogeometric analysis’. In: *Optimization and Engineering* (2024), pp. 1–28.
- [22] Thomas JR Hughes, John A Cottrell and Yuri Bazilevs. ‘Isogeometric analysis: CAD, finite elements, NURBS, exact geometry and mesh refinement’. In: *Computer Methods in Applied Mechanics and Engineering* 194.39-41 (2005), pp. 4135–4195.
- [23] Chun Kit Jeffery Hou and Kamran Behdinan. ‘Dimensionality reduction in surrogate modeling: A review of combined methods’. In: *Data Science and Engineering* 7.4 (2022), pp. 402–427.
- [24] Mengyu Cheng et al. ‘A review of data-driven surrogate models for design optimization of electric motors’. In: *IEEE Transactions on Transportation Electrification* (2024).
- [25] JSOL Corporation. *JMAG-RT Model Library*. 2024. URL: <https://www.jmag-international.com/modellibrary/>.

- [26] Michael Wiesheu. *MotorOptimization*. Nov. 2023. DOI: 10.5281/zenodo.10160086.
- [27] Rafael Vázquez. ‘A new design for the implementation of isogeometric analysis in Octave and Matlab: GeoPDEs 3.0’. In: *Computers & Mathematics with Applications* 72.3 (2016), pp. 523–554.
- [28] Les Piegl and Wayne Tiller. *The NURBS Book*. Springer Science & Business Media, 2012.
- [29] Annalisa Buffa et al. ‘Approximation estimates for isogeometric spaces in multipatch geometries’. In: *Numerical Methods for Partial Differential Equations* 31.2 (2015), pp. 422–438.
- [30] Herbert Egger et al. ‘On torque computation in electric machine simulation by harmonic mortar methods’. In: *Journal of Mathematics in Industry* 12.1 (2022), p. 6.
- [31] Zeger Bontinck et al. ‘Isogeometric analysis and harmonic stator–rotor coupling for simulating electric machines’. In: *Computer Methods in Applied Mechanics and Engineering* 334 (2018), pp. 40–55.
- [32] David C Meeker. ‘Finite element method magnetics, version 4.2 (28feb2018 build)’. In: *URL: <http://www.femm.info>* (2019).
- [33] Zeger Bontinck, Herbert De Gersem and Sebastian Schöps. ‘Response surface models for the uncertainty quantification of eccentric permanent magnet synchronous machines’. In: *IEEE Transactions on Magnetics* 52.3 (2015), pp. 1–4.
- [34] Peter Offermann et al. ‘Uncertainty quantification and sensitivity analysis in electrical machines with stochastically varying machine parameters’. In: *IEEE Transactions on Magnetics* 51.3 (2015), pp. 1–4.
- [35] Armin Galetzka et al. ‘A multilevel Monte Carlo method for high-dimensional uncertainty quantification of low-frequency electromagnetic devices’. In: *IEEE Transactions on Magnetics* 55.8 (2019), pp. 1–12.
- [36] Andres Beltran-Pulido et al. ‘Uncertainty quantification and sensitivity analysis in a nonlinear finite-element model of a permanent magnet synchronous machine’. In: *IEEE Transactions on Energy Conversion* 35.4 (2020), pp. 2152–2161.
- [37] Ion Gabriel Ion et al. ‘Robust shape optimization of electric devices based on deterministic optimization methods and finite-element analysis with affine parametrization and design elements’. In: *Electrical Engineering* 100.4 (2018), pp. 2635–2647.
- [38] Gang Lei et al. ‘Robust design optimization of electrical machines: Multi-objective approach’. In: *IEEE Transactions on Energy Conversion* 36.1 (2020), pp. 390–401.
- [39] Gerd Bramerdorfer. ‘Multiobjective electric machine optimization for highest reliability demands’. In: *CES Transactions on Electrical Machines and Systems* 4.2 (2020), pp. 71–78.
- [40] Dongbin Xiu and George Em Karniadakis. ‘The Wiener–Askey polynomial chaos for stochastic differential equations’. In: *SIAM Journal on Scientific Computing* 24.2 (2002), pp. 619–644.
- [41] Jonathan Feinberg, Vinzenz Gregor Eck and Hans Petter Langtangen. ‘Multivariate polynomial chaos expansions with dependent variables’. In: *SIAM Journal on Scientific Computing* 40.1 (2018), A199–A223.
- [42] Nora Lüthen, Stefano Marelli and Bruno Sudret. ‘Sparse polynomial chaos expansions: Literature survey and benchmark’. In: *SIAM/ASA Journal on Uncertainty Quantification* 9.2 (2021), pp. 593–649.
- [43] Géraud Blatman and Bruno Sudret. ‘Adaptive sparse polynomial chaos expansion based on least angle regression’. In: *Journal of Computational Physics* 230.6 (2011), pp. 2345–2367.
- [44] Stefano Marelli and Bruno Sudret. ‘UQLab: A framework for uncertainty quantification in Matlab’. In: *Vulnerability, Uncertainty, and Risk: Quantification, Mitigation, and Management*. 2014, pp. 2554–2563.

- [45] Léon Bottou, Frank E Curtis and Jorge Nocedal. ‘Optimization methods for large-scale machine learning’. In: *SIAM Review* 60.2 (2018), pp. 223–311.
- [46] Atilim Gunes Baydin et al. ‘Automatic differentiation in machine learning: a survey’. In: *Journal of Machine Learning Research* 18.153 (2018), pp. 1–43.
- [47] Martín Abadi et al. ‘Tensorflow: Large-scale machine learning on heterogeneous distributed systems’. In: *arXiv preprint arXiv:1603.04467* (2016).
- [48] Christopher KI Williams and Carl Edward Rasmussen. *Gaussian Processes for Machine Learning*. Vol. 2. 3. MIT Press Cambridge, MA, 2006.
- [49] Nikolaus Hansen and Andreas Ostermeier. ‘Completely derandomized self-adaptation in evolution strategies’. In: *Evolutionary Computation* 9.2 (2001), pp. 159–195.
- [50] Haitao Liu, Jianfei Cai and Yew-Soon Ong. ‘Remarks on multi-output Gaussian process regression’. In: *Knowledge-Based Systems* 144 (2018), pp. 102–121.
- [51] Hervé Abdi and Lynne J Williams. ‘Principal component analysis’. In: *Wiley Interdisciplinary Reviews: Computational Statistics* 2.4 (2010), pp. 433–459.
- [52] Katiana Kontolati et al. ‘Learning nonlinear operators in latent spaces for real-time predictions of complex dynamics in physical systems’. In: *Nature Communications* 15.1 (2024), p. 5101.

Appendix

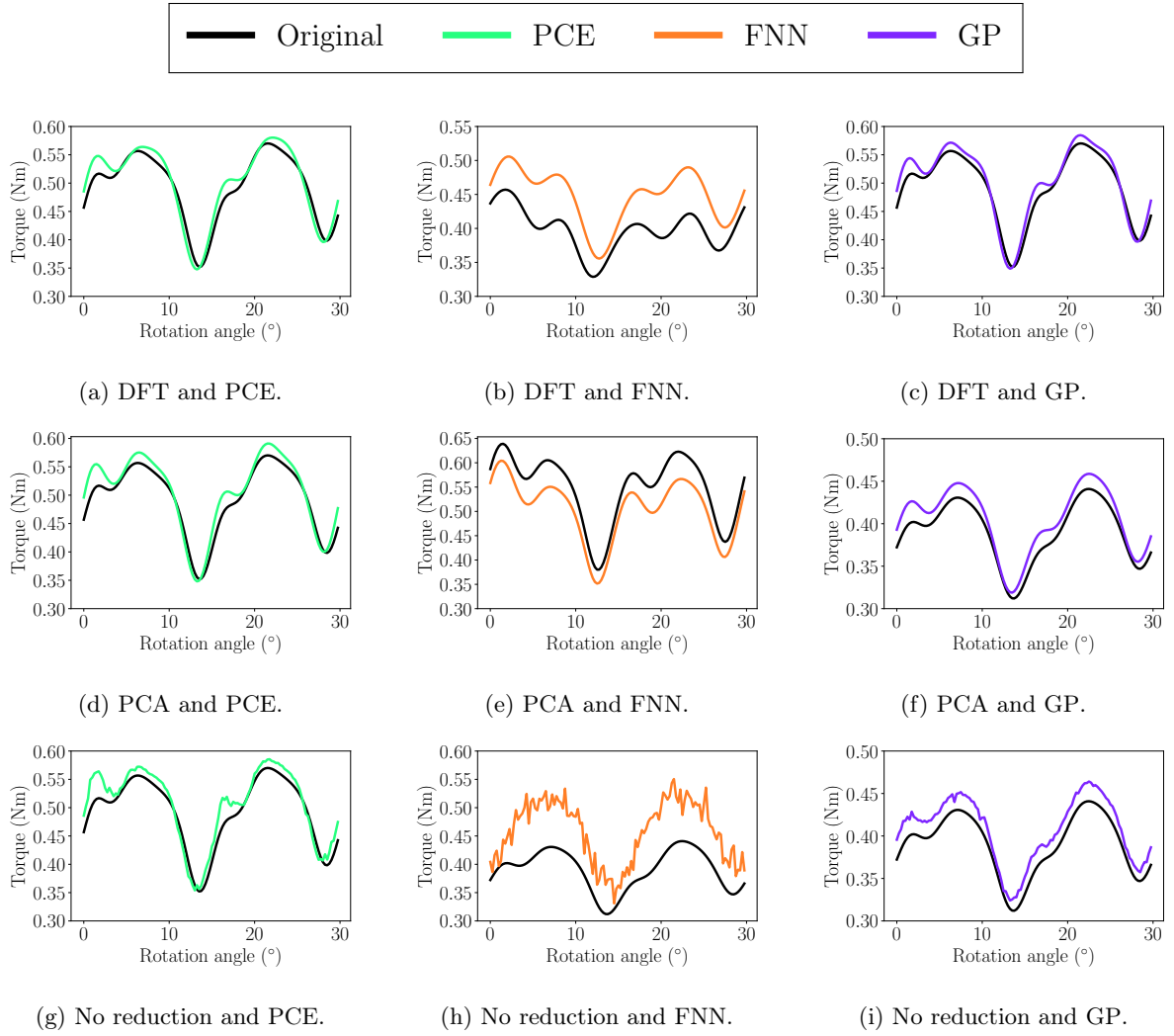


Figure 9: Worst-case surrogate-based torque signal signal predictions for training dataset size $M_t = 600$ and different combinations of RSM and dimension reduction approach.

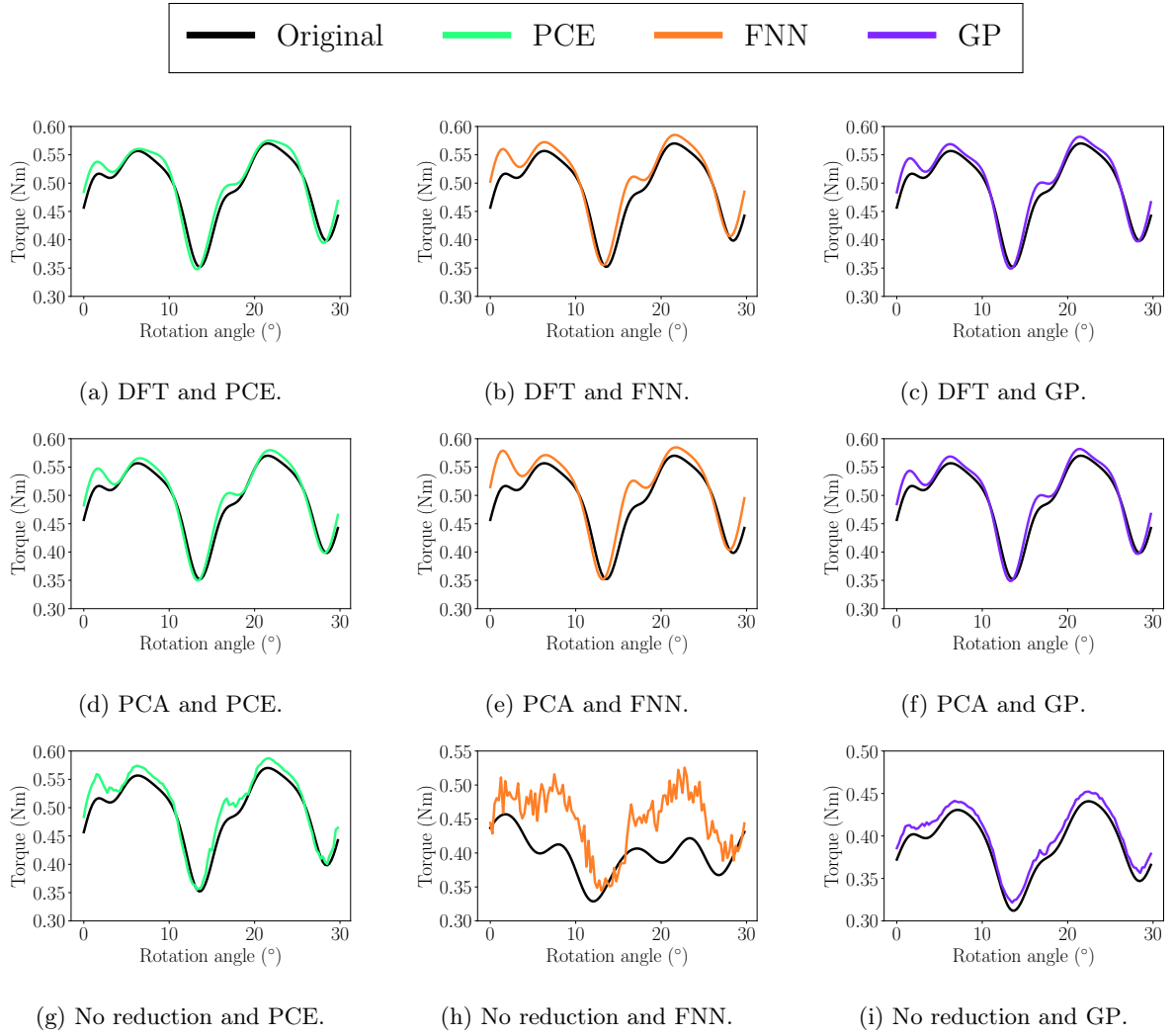


Figure 10: Worst-case surrogate-based torque signal predictions for training dataset size $M_t = 1200$ and different combinations of RSM and dimension reduction approach.